

Analysis of the spatiotemporal velocity of annual precipitation based on random field

Chenlong Li & Yang Hu

To cite this article: Chenlong Li & Yang Hu (31 Mar 2024): Analysis of the spatiotemporal velocity of annual precipitation based on random field, Communications in Statistics - Theory and Methods, DOI: [10.1080/03610926.2024.2330678](https://doi.org/10.1080/03610926.2024.2330678)

To link to this article: <https://doi.org/10.1080/03610926.2024.2330678>



Published online: 31 Mar 2024.



Submit your article to this journal [↗](#)



Article views: 10



View related articles [↗](#)



View Crossmark data [↗](#)



Analysis of the spatiotemporal velocity of annual precipitation based on random field

Chenlong Li^a and Yang Hu^a

^aSchool of Mathematics, Taiyuan University of Technology, Taiyuan, China

ABSTRACT

Changes in precipitation directly impact river runoff volume, subsequently influencing food production, and the security of downstream urban areas. In this study, we introduce a random velocity field (RVF) capable of performing multi-step predictions while providing interpretable insights into precipitation variations. The RVF leverages the gradient of a Gaussian random field to learn spatiotemporal velocity patterns and employs a predictive process to reduce dimensionality and enable multi-step forecasting. Bayesian parameter estimation is obtained using the Markov Chain Monte Carlo (MCMC) method. Our analysis reveals a noticeable shifting trend in annual precipitation based on diverse real datasets. This trend serves as a valuable foundation for further exploration of urban flood control and agricultural development strategies.

ARTICLE HISTORY

Received 15 January 2023
Accepted 09 March 2024

KEYWORDS

Gaussian random field;
Markov chain Monte Carlo
method; spatiotemporal
velocity; annual precipitation

1. Introduction

Precipitation observations are fundamental in water resource management, exerting substantial influence over industrial and agricultural production, water resource development, river flood control, and project management. The study of precipitation has garnered notable attention in recent years, with a central focus on three key facets: unraveling the spatiotemporal characteristics of extreme precipitation events, elucidating the driving factors behind precipitation patterns, and studying the ramifications of high-intensity precipitation.

Research by Zhang, Hogg, and Éva (2001) comprehensively analyzed extreme precipitation events in Canada from 1900 to 1998, providing valuable insights into the spatiotemporal characteristics of these events. Sebille, Fougères, and Mercadier (2017) adopted a different approach by selecting five spatial models and incorporating Bayesian and frequentist concepts to analyze real precipitation datasets in central and eastern France. Their comparative study highlighted the distinctive properties of each model and provided valuable insights into model selection for specific risk types. Richards, Tawn, and Brown (2023) further contributed to our understanding of extreme precipitation by employing a mixed model to estimate spatially aggregated precipitation at different scales jointly. They emphasized the importance of capturing aggregated precipitation across river catchments, highlighting the significance of accounting for precipitation-induced variations in flood risk assessments. Majumder and Reich (2023) similarly underscored the significance of precipitation in contributing to the

spatial and temporal variability of extreme flows, which directly impacts current and future flood risk assessments. Their work emphasized the need to consider precipitation-induced variations when evaluating flood risk.

Understanding the drivers behind precipitation patterns is vital for accurate prediction and preparedness for extreme events. Researchers have scrutinized various aspects of precipitation. For example, Marques, Klein, and Kneib (2020) explored the influence of topography and the non stationarity of precipitation phenomena, highlighting the role of factors like wind in causing directional dependence. Rui et al. (2020b) identified driving factors affecting precipitation patterns in the Tianshan region of China, while Ribas, Olcina, and Sauri (2020) conducted a comprehensive study on the impact of high-intensity precipitation on flood vulnerability in the Mediterranean region of Spain, advocating for a holistic vulnerability analysis method. Mahbod and Rafiee (2021) analyzed trends in extreme precipitation events in Iran using the percentile index. In addition, Fischer, Rust, and Ulbrich (2019) conducted a study that emphasized the ramifications of extreme precipitation events. These events pose a threat in two main ways: directly, in the form of phenomena like hail, freezing rain, or flash floods, and indirectly, through processes like increased erosion, mudslides, or river flooding. The seasonality of extreme precipitation is significant, as seasonal cycles of extreme precipitation can profoundly impact crop yields, especially during the vulnerable early stages of the growing season. Their study provided detailed insights by offering monthly resolved return levels for gauged and ungauged sites. They achieved this by modeling spatial and seasonal precipitation extremes in the Berlin-Brandenburg region of Germany. This research contributes valuable information for understanding the region's dynamics and consequences of extreme precipitation events.

However, more than focusing solely on precipitation intensity is required. Climate change, particularly rising temperatures, has led to variations in precipitation trends across regions, with some experiencing increasing or decreasing precipitation over the years (Villarini, Smith, and Napolitano 2010; Rusticucci et al. 2010). These changes manifest as alterations in precipitation intensity in both spatial and temporal dimensions, termed the spatiotemporal velocity of precipitation intensity. This phenomenon has ecological implications, as it can influence the habitats of plants and animals. When precipitation intensity changes gradually, plant and animal habitats remain relatively stable. However, when changes are abrupt, the risk of droughts or floods arises, prompting potential plant and animal species migrations in response to spatiotemporal velocity shifts. Therefore, studying the spatiotemporal velocity of precipitation intensity is of paramount practical significance. Regrettably, this aspect has received limited attention.

In contrast, considerable research has been devoted to other climate changes, particularly temperature shifts. Studies by Furey et al. (2012) and Holsinger et al. (2014) have delved into the impact of temperature-dominated climate changes on landscapes. Sloat et al. (2005) assessed ecological suitability by studying river temperatures, while Loarie et al. (2009) investigated how temperature changes affect the activities of plants and animals. Schliep, Gelfand, and Clark (2015) explored the relationship between the speed of climate change and temperature variations. These factors mentioned above, including topography, geographical location, temperature, and time, collectively influence the spatiotemporal velocity of annual precipitation intensity. The insights gained from studies on climate change are instructive when considering changes in precipitation intensity. Building upon the spirit of these studies, we aim to predict future trends in precipitation intensity by studying the velocity of precipita-

tion intensity. These predictions can inform flood control and drought prevention measures, ultimately reducing losses.

In this article, we propose an RVF model that incorporates time, longitude, latitude, and spatiotemporal effect factors to accomplish our objectives. This model allows us to analyze annual precipitation intensity and its velocity in six countries across five continents, each in different regions. Through this model, we study the annual precipitation intensity and velocity of six countries on five continents in different regions. The data employed for this analysis consist of annual precipitation intensity datasets for China, the United States, Australia, the Netherlands, India, and Brazil, encompassing information on precipitation observation locations, time, and precipitation intensity. These weather station datasets are highly reliable. The spatiotemporal effect factors within our model are approximated using the Gaussian random field, a mathematical framework with well-established properties inherited from the normal distribution (Gu, Fei, and Sun 2020; Rhode 2020; Liu et al. 2020; Rui et al. 2020a; Sørbye and Rue 2014). Given the high dimensionality of the data, we employ the predictive process to mitigate over-fitting and achieve dimensionality reduction. The predictive process effectively models the initial process realization within a lower-dimensional subspace, reducing computational complexity. Parameter estimation for the annual precipitation intensity RVF model uses the Markov Chain Monte Carlo (MCMC) method (Reis and Stedinger 2005; Mendes, Turkman, and Corte-Real 2006; Sigrist, Künsch, and Stahel 2011), which allows us to study the future precipitation intensity velocity in various regions across the six countries. Our findings indicate that annual precipitation intensity has increased significantly in some countries and regions, leading to an elevated risk of flooding. Therefore, proactive flood control measures should be implemented. Conversely, other areas are susceptible to drought risks, necessitating a focus on environmental conservation, increased vegetation, and improved water storage arrangements. This model offers valuable insights for ensuring food production safety and effective urban flood control measures.

The rest of the article is organized as follows. In [Section 2](#), we introduce the general annual precipitation model and derive annual precipitation models of varying orders using Taylor expansion. In [Section 3](#), we delve into the Bayesian parameter estimation method and provide a detailed derivation of the posterior distribution of parameters. [Section 4](#) is dedicated to describing the simulation experiment conducted in the study. In [Section 5](#), the authors provide an overview of the datasets used, which consist of annual precipitation intensity data from six different regions spanning five continents. [Section 6](#) involves model fitting, parameter estimation for the RVF model, and the analysis of annual precipitation intensity velocity using the RVF model. The article concludes with [Section 7](#).

2. Model

This chapter aims to formulate the RVF model. In [Section 2.1](#), we introduce a general model for annual precipitation. To prevent over-fitting, we apply the prediction process to this model. Subsequently, we conduct an initial exploration of the RVF model. [Section 2.2](#) introduces two annual precipitation models of varying orders derived through Taylor expansion. The order of the annual precipitation model is determined using AIC and BIC criteria. Following this, we present the relevant RVF model and establish the covariance function for the Gaussian process.

2.1. Annual precipitation random field model

This section presents a general model describing annual precipitation intensity at a specific spatiotemporal point (x, y, z, t) , where x, y, z , and t represent longitude, latitude, altitude, and time.

2.1.1. Generalized parameter model

Taking into account various factors, including latitude, longitude, altitude, and time, we propose a generalized model for annual precipitation:

$$P(x, y, z, t) = h(x, y, z, t) + \mathbf{W}(x, y, z)f(t) + \eta(x, y, z, t), \quad (2.1)$$

where $P(x, y, z, t)$ represents the annual precipitation at the point (x, y, z, t) , $h(x, y, z, t)$ signifies a deterministic function capturing the spatiotemporal effect, $\mathbf{W}(x, y, z)$ is a random function accounting for the rate of change in annual precipitation, $f(t)$ is a determined function, $\mathbf{W}(x, y, z)f(t)$ represents the random spatiotemporal effect, and $\eta(x, y, z, t)$ is a random perturbation term characterized by a normal distribution with a mean of 0 and a variance of σ_p^2 and is independent of other terms in the model. Specifically, we use the Gaussian random field to approximate the spatial random effect $\mathbf{W}(x, y, z)$, a commonly utilized approach known for its favorable results across various scenarios.

2.1.2. Predictive process

Given the uneven spatial distribution of monitoring sites, correlations emerge in the annual precipitation across certain areas. Moreover, over-fitting becomes a concern when dealing with high-dimensional data, potentially resulting in unsatisfactory model fitting and prediction results. As a solution, we adopt the predictive process (Banerjee et al. 2008) within formula (2.1) to mitigate correlations and prevent over-fitting while retaining as much of the original information as possible. This involves standardizing the geographical locations using the predictive process and projecting them onto a designated coordinate, typically an isometric grid point.

The predictive process is integrated into the model (2.1), yielding the formulation

$$P(x, y, z, t) = h(x, y, z, t) + \tilde{\mathbf{W}}(x, y, z)f(t) + \eta(x, y, z, t), \quad (2.2)$$

with $\tilde{\mathbf{W}}(x, y, z)$ being represented as the Gaussian predictive process denoted by $\mathbb{E}(\mathbf{W}(x, y, z)|\mathbf{W}^*) = C'_{\mathbf{W}, \mathbf{W}^*} (C_{\mathbf{W}^*})^{-1} \mathbf{W}^*$. This predictive process serves as spatial interpolation through a dimension reduction process $\mathbf{W}^* = [\mathbf{W}(x_1^*, y_1^*, z_1^*), \dots, \mathbf{W}(x_m^*, y_m^*, z_m^*)]'$. \mathbf{W}^* denotes a spatial process on a lower-dimensional subspace, where (x_j^*, y_j^*, z_j^*) , $j = 1, \dots, m$ are the positions of the nodes. To elaborate, $\mathbf{W}(x, y, z)$ is projected onto \mathbf{W}^* within this lower dimension. By examining the relationship between $\tilde{\mathbf{W}}(x, y, z)$ and $\mathbf{W}(x, y, z)$ and \mathbf{W}^* , it is evident that the covariance of $\tilde{\mathbf{W}}(x, y, z)$ is $C'_{\mathbf{W}, \mathbf{W}^*} (C_{\mathbf{W}^*})^{-1} C_{\mathbf{W}, \mathbf{W}^*}$, where $(C_{\mathbf{W}, \mathbf{W}^*})_j = \text{Cov}(\mathbf{W}(x, y, z), \mathbf{W}(x_j^*, y_j^*, z_j^*))$, $(C_{\mathbf{W}^*})_{ij} = \text{Cov}(\mathbf{W}(x_i^*, y_i^*, z_i^*), \mathbf{W}(x_j^*, y_j^*, z_j^*))$, $i, j = 1, \dots, m$.

The chosen covariance function for the predictive process is the Matérn class covariance function, a fundamental component in spatial statistics. With the continuous evolution of spatiotemporal data modeling, there is an increasing need for in-depth theoretical research on spatiotemporal covariance structures. The selection of the Matérn model is primarily motivated by its parameter ν , which governs the smoothness of the random field. A higher ν value leads to a smoother random field. Despite the control parameters, the smooth random

field retains flexibility, a crucial aspect of spatial interpolation. It's worth noting that the model is m order mean-square differentiable only when $\nu > m$. If ν is non integer and equals $\frac{1}{2} + m$, the model is said to be rational.

2.1.3. The RVF

Building upon the established annual precipitation model and drawing from the studies by Furey et al. (2012); Holsinger et al. (2014); Sloat et al. (2005); Loarie et al. (2009); Schliep, Gelfand, and Clark (2015) as references, we introduce the following random velocity field (RVF).

Based on the main part of Equation (2.2), we propose the RVF. Taking the conditional expectation of annual precipitation $P(x, y, z, t)$ in Equation (2.2), we obtain

$$R(x, y, z, t) = \mathbb{E}(P(x, y, z, t) | \mathbf{W}^*) = h(x, y, z, t) + \tilde{\mathbf{W}}(x, y, z) f(t). \quad (2.3)$$

In Equation (2.3), $R(x, y, z, t)$ is a realization of a random process and is mean-square differentiable. Calculating the temporal and spatial gradient at time t and position (x, y, z) , respectively, one has the velocity in unit direction $u = [u_x, u_y, u_z]'$ as follows:

$$\frac{\frac{\partial R(x, y, z, t)}{\partial t}}{\nabla R(x, y, z, t) u} = \frac{\frac{\partial R(x, y, z, t)}{\partial t}}{\frac{\partial R(x, y, z, t)}{\partial x} u_x + \frac{\partial R(x, y, z, t)}{\partial y} u_y + \frac{\partial R(x, y, z, t)}{\partial z} u_z},$$

where $u_x^2 + u_y^2 + u_z^2 = 1$, $\frac{\partial R(x, y, z, t)}{\partial x}$, $\frac{\partial R(x, y, z, t)}{\partial y}$, $\frac{\partial R(x, y, z, t)}{\partial z}$, and $\frac{\partial R(x, y, z, t)}{\partial t}$ are partial derivatives in the x, y, z , and t directions, respectively, $\nabla R(x, y, z, t) u$ represents the gradient in direction u and $\nabla R(x, y, z, t) = [\frac{\partial R(x, y, z, t)}{\partial x}, \frac{\partial R(x, y, z, t)}{\partial y}, \frac{\partial R(x, y, z, t)}{\partial z}]$ represents the spatial gradient of annual precipitation.

For instance, the temporal gradient represents the time velocity of annual precipitation, and the spatial gradient represents the space velocity of annual precipitation. The annual precipitation velocity, measured in kilometers per year, is the temporal and spatial gradient ratio. The velocity in direction u is the ratio of the Gaussian random field, which is also a Gaussian random field.

The direction with the maximum unit gradient is denoted by $\frac{\nabla R(x, y, z, t)}{\|\nabla R(x, y, z, t)\|}$, where $\|\nabla R(x, y, z, t)\|$ represents the magnitude of the maximum gradient. The minimum rate of velocity corresponds to the velocity in the unit direction of the maximum gradient, that is,

$$\frac{\frac{\partial R(x, y, z, t)}{\partial t}}{\|\nabla R(x, y, z, t)\|}. \quad (2.4)$$

As the numerator can be either positive or negative, the velocity can also be positive or negative. When the ratio is positive, the change in annual precipitation along the direction of the maximum gradient is the minimum; conversely, when the ratio is negative, the change in annual precipitation in the direction opposite to the direction of the maximum gradient is the minimum.

2.2. Model parameterization

To parameterize model (2.1), we initiate a Taylor expansion of its components at zero, that is,

$$\begin{aligned}
 h(x, y, z, t) &= \sum_{i=0}^{\infty} \frac{1}{i!} \left(x \frac{\partial}{\partial x} + y \frac{\partial}{\partial y} + z \frac{\partial}{\partial z} + t \frac{\partial}{\partial t} \right)^i h(0, 0, 0, 0) \\
 &\approx \sum_{i=0}^p \frac{1}{i!} \left(x \frac{\partial}{\partial x} + y \frac{\partial}{\partial y} + z \frac{\partial}{\partial z} + t \frac{\partial}{\partial t} \right)^i h(0, 0, 0, 0) \\
 &= \sum_{i=0}^p \sum_{\substack{j_1+j_2+j_3+j_4=i \\ j_1, j_2, j_3, j_4 \in \mathbb{N}}} \beta_{j_1, j_2, j_3, j_4} x^{j_1} y^{j_2} z^{j_3} t^{j_4} \frac{1}{i!} \\
 &= \mathbf{X} \boldsymbol{\beta}',
 \end{aligned} \tag{2.5}$$

and

$$\begin{aligned}
 f(t) &= \sum_{i=0}^{\infty} \frac{t^i}{i!} f^{(i)}(0) \\
 &\approx \sum_{i=0}^q \frac{t^i}{i!} f^{(i)}(0) \\
 &= \mathbf{t} \boldsymbol{\alpha}',
 \end{aligned} \tag{2.6}$$

where $\boldsymbol{\beta} = [\beta_1, \dots, \beta_p]_{1 \times M}$, $M = \sum_{i=0}^p 4^i$, $\beta_i = [\beta_{i,0,0,0}, \dots, \beta_{0,0,0,i}]_{1 \times 4^i}$ is the Taylor expansion coefficient of order i , $\mathbf{X} = [X_1, \dots, X_p]_{1 \times M}$, $X_i = \frac{1}{i!} [x^i y^0 z^0 t^0, \dots, x^0 y^0 z^0 t^i]_{1 \times 4^i}$, $\mathbf{t} = [\frac{t^0}{0!}, \dots, \frac{t^q}{q!}]_{1 \times (q+1)}$, $\boldsymbol{\alpha} = [f'(0), \dots, f^{(q)}(0)]_{1 \times (q+1)}$.

By substituting Equations (2.5) and (2.6) into the model (2.1), we obtain the generalized parameter model as follows:

$$P(x, y, z, t) = \mathbf{X} \boldsymbol{\beta}' + \mathbf{W}(x, y, z) \mathbf{t} \boldsymbol{\alpha}' + \eta(x, y, z, t). \tag{2.7}$$

In Equation (2.7), the order of Equation (2.7) grows exponentially (order 4^i) due to the dimension expansion issue. Consequently, this article explores models where $p, q \in \{0, 1\}$, and we select the optimal p and q using AIC and BIC criteria. The expressions for the models with $p, q \in \{0, 1\}$ are as follows:

$$\begin{aligned}
 P_0(x, y, z, t) &= \beta_0 + \mathbf{W}_1(x, y, z) + \eta(x, y, z, t) \\
 &= \mathbf{X}_0 \boldsymbol{\beta}^0 + \mathbf{W}_1(x, y, z) + \eta(x, y, z, t),
 \end{aligned} \tag{2.8}$$

and

$$\begin{aligned}
 P_1(x, y, z, t) &= \beta_0 + \beta_1 x + \beta_2 y + \beta_3 z + \beta_4 t + \mathbf{W}_1(x, y, z) + \mathbf{W}_2(x, y, z) t + \eta(x, y, z, t) \\
 &= \mathbf{X}_1 \boldsymbol{\beta}^1 + \mathbf{W}_1(x, y, z) + \mathbf{W}_2(x, y, z) t + \eta(x, y, z, t),
 \end{aligned} \tag{2.9}$$

where $\mathbf{X}_0 = [L]$, $\mathbf{X}_1 = [L, x, y, z, t]$, L is an n -dimensional column vector with all 1's, n is the data size, and $\boldsymbol{\beta}^0 = \beta_0$, $\boldsymbol{\beta}^1 = [\beta_0, \beta_1, \beta_2, \beta_3, \beta_4]^\top$. Applying the predictive process to these two models, we find that

$$P_0(x, y, z, t) = \mathbf{X}_0 \boldsymbol{\beta}^0 + \tilde{\mathbf{W}}_1(x, y, z) + \eta(x, y, z, t), \tag{2.10}$$

and

$$P_1(x, y, z, t) = \mathbf{X}_1\beta^1 + \tilde{\mathbf{W}}_1(x, y, z) + \tilde{\mathbf{W}}_2(x, y, z)t + \eta(x, y, z, t), \quad (2.11)$$

where $\tilde{\mathbf{W}}_1(x, y, z) = \mathbb{E}(\mathbf{W}_1(x, y, z)|\mathbf{W}_1^*) = C'_{\mathbf{W}_1, \mathbf{W}_1^*} (C_{\mathbf{W}_1^*})^{-1} \mathbf{W}_1^*$ and $\tilde{\mathbf{W}}_2(x, y, z) = \mathbb{E}(\mathbf{W}_2(x, y, z)|\mathbf{W}_2^*) = C'_{\mathbf{W}_2, \mathbf{W}_2^*} (C_{\mathbf{W}_2^*})^{-1} \mathbf{W}_2^*$. Subsequently, the corresponding RVF models based on the aforementioned predictive processes are as follows:

$$R_0(x, y, z, t) = \mathbf{X}_0\beta^0 + \tilde{\mathbf{W}}_1(x, y, z), \quad (2.12)$$

and

$$R_1(x, y, z, t) = \mathbf{X}_1\beta^1 + \tilde{\mathbf{W}}_1(x, y, z) + \tilde{\mathbf{W}}_2(x, y, z)t. \quad (2.13)$$

It's worth noting that the RVF model (2.12) can be viewed as a special case of the RVF model (2.13). Therefore, we will focus on the results derived from the RVF model (2.13) in the subsequent analysis. To compute the gradient in detail for the RVF model (2.13), let S^* and Q^* represent the $m \times m$ autocorrelation matrices of \mathbf{W}_1^* and \mathbf{W}_2^* , respectively. Specifically, $S_{ij}^* = \rho(d_{ij}; \phi_1)$ and $Q_{ij}^* = \rho(d_{ij}; \phi_0)$, where ϕ_1 and ϕ_0 are attenuation parameters, and $i, j = 1, \dots, m$. Let $s(x, y, z)$ and $q(x, y, z)$ denote the cross-correlation vectors of size $m \times 1$, where $s_i(x, y, z)$ represents the correlation between $\mathbf{W}_1(x, y, z)$ and $\mathbf{W}_1(x_i^*, y_i^*, z_i^*)$, $i = 1, \dots, m$, and $q_i(x, y, z)$ signifies the correlation between $\mathbf{W}_2(x, y, z)$ and $\mathbf{W}_2(x_i^*, y_i^*, z_i^*)$, for $i = 1, \dots, m$. Additionally, let $\beta^* = [\beta_1, \beta_2, \beta_3]^\top$, $\nabla s^T(x, y, z) = [\frac{\partial s^T(x, y, z)}{\partial x}, \frac{\partial s^T(x, y, z)}{\partial y}, \frac{\partial s^T(x, y, z)}{\partial z}]^\top$, $\nabla q^T(x, y, z) = [\frac{\partial q^T(x, y, z)}{\partial x}, \frac{\partial q^T(x, y, z)}{\partial y}, \frac{\partial q^T(x, y, z)}{\partial z}]^\top$. Then, the spatial gradient $\nabla R(x, y, z, t)^\top$ of annual precipitation can be determined using the following formulas:

$$\nabla R(x, y, z, t)^\top = \beta^* + \nabla s^T(x, y, z)S^{*-1}\mathbf{W}_1^* + \nabla q^T(x, y, z)Q^{*-1}\mathbf{W}_2^*t. \quad (2.14)$$

The temporal gradient of annual precipitation is represented as

$$\frac{\partial R(x, y, z, t)}{\partial t} = \beta_4 + q^T(x, y, z)Q^{*-1}\mathbf{W}_2^*. \quad (2.15)$$

Equation (2.14) provides the velocity of annual precipitation per unit distance in the x , y , and z directions. The spatial gradient follows a Gaussian random field distribution. Notably, the temporal gradient (2.15) is characterized as a Gaussian process, and its covariance can be readily computed. Since the formula (2.15) lacks a time component, it can be considered a simple surface. To ensure the first-order mean square differentiability of the RVF model, we select the Matérn model with $\nu = 3/2$.

A strong spatial correlation exists among annual precipitation levels in different regions, with closer distances exhibiting higher correlation coefficients. This spatial relationship can be expressed through a covariance matrix. For any two positions (x_i, y_i, z_i) and (x_j, y_j, z_j) , the covariance of $\mathbf{W}_1(x_i, y_i, z_i)$ and $\mathbf{W}_1(x_j, y_j, z_j)$ is

$$\text{Cov}(\mathbf{W}_1(x_i, y_i, z_i), \mathbf{W}_1(x_j, y_j, z_j)) = \tau_1^2(1 + \phi_1 d_{ij} \exp(-\phi_1 d_{ij})),$$

and the covariance of $\mathbf{W}_2(x_i, y_i, z_i)$ and $\mathbf{W}_2(x_j, y_j, z_j)$ is

$$\text{Cov}(\mathbf{W}_2(x_i, y_i, z_i), \mathbf{W}_2(x_j, y_j, z_j)) = \tau_0^2(1 + \phi_0 d_{ij} \exp(-\phi_0 d_{ij})),$$

where d_{ij} represents the distance between (x_i, y_i, z_i) and (x_j, y_j, z_j) , ϕ_1 and ϕ_0 are the spatial attenuation parameters, τ_1^2 and τ_0^2 are the spatial variance parameters, which do not play a role in subsequent parameter estimation and are therefore set to 1 for computational convenience.

Once the covariance function is determined, we can calculate the spatial gradient of annual precipitation. Initially, we compute the derivatives of $s_j(x, y, z)$ and $q_j(x, y, z)$, where $j = 1, \dots, m$, concerning x, y and z . Let

$$\nabla s_j(x, y, z) = \left[\frac{\partial s_j(x, y, z)}{\partial x}, \frac{\partial s_j(x, y, z)}{\partial y}, \frac{\partial s_j(x, y, z)}{\partial z} \right],$$

$$\nabla q_j(x, y, z) = \left[\frac{\partial q_j(x, y, z)}{\partial x}, \frac{\partial q_j(x, y, z)}{\partial y}, \frac{\partial q_j(x, y, z)}{\partial z} \right],$$

and

$$A_i = \text{diag}(\phi_i^2 \exp(-\phi_i d), \phi_i^2 \exp(-\phi_i d), \phi_i^2 \exp(-\phi_i d)), i = 0, 1.$$

The derivatives of $s_j(x, y, z)$, $q_j(x, y, z)$ with respect to x, y and z are given by

$$[\nabla s_j(x, y, z), \nabla q_j(x, y, z)] = -[c, c] \begin{pmatrix} A_1 & 0 \\ 0 & A_0 \end{pmatrix}.$$

where $c = (x - x_j^*, y - y_j^*, z - z_j^*)$ and $d = \|c\|$.

3. Bayesian parameter estimation

3.1. Markov Chain Monte Carlo method

A Markov chain is a discrete random variable set that exhibits the Markov property. Specifically, for the sequence of random variables denoted as $X = \{X_n, n > 0\}$ within the probability space (Ω, F, P) , where the sample space is an exponential set, if the values of these random variables all belong to a countable set: $X = s_i$, where $s_i \in s$, and if the conditional probability of a random variable satisfies the relation:

$$p(X_{t+1}|X_t, \dots, X_1) = p(X_{t+1}|X_t),$$

then X is called a Markov chain. The countable set s , a subset of the integers (Z), is termed the state space, and the values that the Markov chain takes within this state space are referred to as states. The equation above defines a Markov chain and encapsulates the Markov property, often called "memorylessness". It implies that the random variable at time $t + 1$ is independent of the other random variables beyond time t , given the random variable at time t .

Markov chains find application in the Monte Carlo method to create Markov Chain Monte Carlo (MCMC). In this context, if Ω denotes a particular space, n signifies the total number of generated samples, m represents the number of samples at which the chain attains stability, and x is the parameter to be estimated, the fundamental concept of the MCMC method can be briefly summarized as follows:

(1) Construct a Markov Chain: Formulate a Markov chain designed to converge to a stationary distribution, denoted as $\pi(x)$.

(2) Sample Generation: Commencing from a point $x^{(0)}$ within Ω , employ the Markov chain from step (1) for simulating samples, generating a sequence of points: $x^{(1)}, \dots, x^{(n)}$.

(3) Monte Carlo Integral: Estimate the expected value of any function $f(x)$ as $E[f(t)] = \frac{1}{n-m} \sum_{t=m+1}^n f(x^{(t)})$.

The construction of the Markov chain transfer kernel is essential for the MCMC method. Different transfer kernel produces different MCMC methods. One widely utilized MCMC

method is Gibbs sampling, while a more general approach is the Metropolis-Hastings method. MCMC facilitates transforming a given probability distribution, $\pi(x)$, into a stable distribution.

3.2. Derivation of posterior distributions

In the context of the RVF model (2.13), where $\theta = [\beta, \phi_1, \phi_0, \mathbf{W}_1^*, \mathbf{W}_2^*, \sigma_p^2]$ represents the parameter vector and $P = [P_1, \dots, P_T]$ represents the sample, with $P_t = [P(x_1, y_1, z_1, t), \dots, P(x_n, y_n, z_n, t)]'$ being the annual precipitation observed at n locations over time t , the joint distribution of P and parameter θ can be expressed as $f(P, \theta) = f(P|\theta)\pi(\theta) = f(\theta|P)f(P)$. Consequently, we derive the posterior distribution of θ , denoted as $f(\theta|P) = \frac{f(P|\theta)\pi(\theta)}{f(P)} \propto f(P|\theta)\pi(\theta)$, given that $f(P)$ does not carry any information about θ .

For the parameters $\beta = [\beta_0, \beta_1, \beta_2, \beta_3, \beta_4]'$, ϕ_1 , ϕ_0 , \mathbf{W}_1^* , \mathbf{W}_2^* , and σ_p^2 , non informative conjugate prior distributions have been assigned to all the hyperparameters. Specifically, the coefficients β_k , $k = 0, 1, 2, 3, 4$, are independent and follow a common normal prior distribution with a mean of zero and a variance of 10^4 . The variance σ_p^2 of the error term $\eta(x, y, z, t)$ follows a non informative conjugate inverse gamma $IG(2, 2)$ prior distribution. The spatial attenuation parameters ϕ_1 and ϕ_0 are subject to a uniform prior distribution bounded by the minimum and maximum distances observed at the sites. Therefore, the complete posterior distribution for all parameters is represented as

$$\begin{aligned} \pi(\theta|P) = \pi(\beta, \mathbf{W}_1^*, \mathbf{W}_2^*, \phi_1, \phi_0, \sigma_p^2|P) &\propto \prod_{t=1}^T \pi(P_t|\beta, \mathbf{W}_1^*, \mathbf{W}_2^*, \phi_1, \phi_0, \sigma_p^2) \\ &\times \pi(\beta, \mathbf{W}_1^*, \mathbf{W}_2^*, \phi_1, \phi_0, \sigma_p^2). \end{aligned} \quad (3.1)$$

Since β , ϕ_1 , ϕ_0 , σ_p^2 are independent, Equation (3.1) is equivalent to

$$\begin{aligned} &\prod_{t=1}^T \pi(P_t|\beta, \mathbf{W}_1^*, \mathbf{W}_2^*, \phi_1, \phi_0, \sigma_p^2) \times \pi(\mathbf{W}_1^*, \phi_1) \cdot \pi(\mathbf{W}_2^*, \phi_0) \cdot \pi(\beta) \cdot \pi(\sigma_p^2) \\ &\propto \prod_{t=1}^T \pi(P_t|\beta, \mathbf{W}_1^*, \mathbf{W}_2^*, \phi_1, \phi_0, \sigma_p^2) \times \pi(\mathbf{W}_1^*|\phi_1) \cdot \pi(\phi_1) \cdot \pi(\mathbf{W}_2^*|\phi_0) \cdot \pi(\phi_0) \cdot \pi(\beta) \cdot \pi(\sigma_p^2) \\ &= \prod_{t=1}^T \pi(P_t|\beta, \mathbf{W}_1^*, \mathbf{W}_2^*, \phi_1, \phi_0, \sigma_p^2) \times \pi(\mathbf{W}_1^*|\phi_1) \cdot \pi(\mathbf{W}_2^*|\phi_0) \cdot \pi(\beta, \phi_1, \phi_0, \sigma_p^2), \end{aligned}$$

that is,

$$\begin{aligned} \pi(\theta|P) &= \pi(\beta, \mathbf{W}_1^*, \mathbf{W}_2^*, \phi_1, \phi_0, \sigma_p^2|P) \\ &\propto \prod_{t=1}^T \pi(P_t|\beta, \mathbf{W}_1^*, \mathbf{W}_2^*, \phi_1, \phi_0, \sigma_p^2) \times \pi(\mathbf{W}_1^*|\phi_1) \times \pi(\mathbf{W}_2^*|\phi_0) \times \pi(\beta, \phi_1, \phi_0, \sigma_p^2). \end{aligned}$$

Letting $\Sigma_p = \sigma_p^2 I_n$, $\mathbf{W}_1 = A_{\mathbf{W}_1} \mathbf{W}_1^*$ and $\mathbf{W}_2 = A_{\mathbf{W}_2} \mathbf{W}_2^*$, where Σ_β represents the prior covariance of β , $A_{\mathbf{W}_1} = C'_{\mathbf{W}_1, \mathbf{W}_1^*} (C_{\mathbf{W}_1^*})^{-1}$, $A_{\mathbf{W}_2} = C'_{\mathbf{W}_2, \mathbf{W}_2^*} (C_{\mathbf{W}_2^*})^{-1}$, we can derive the joint

posterior distribution of parameters β , \mathbf{W}_1^* , \mathbf{W}_2^* and σ_p^2 as

$$\begin{aligned} & \pi(\beta, \mathbf{W}_1^*, \mathbf{W}_2^*, \phi_1, \phi_0, \sigma_p^2 | P) \\ & \propto \sum_{t=1}^T |\Sigma_P|^{-1/2} \exp(-1/2(P_t - X_t\beta - \mathbf{W}_1 - \mathbf{W}_2t)^\top \Sigma_P^{-1}(P_t - X_t\beta - \mathbf{W}_1 - \mathbf{W}_2t)) \\ & \quad \times |C_{\mathbf{W}_1^*}|^{-1/2} \exp((-1/2)\mathbf{W}_1^{*\top} C_{\mathbf{W}_1^*}^{-1} \mathbf{W}_1^*) |C_{\mathbf{W}_2^*}|^{-1/2} \exp((-1/2)\mathbf{W}_2^{*\top} C_{\mathbf{W}_2^*}^{-1} \mathbf{W}_2^*) \\ & \quad \times |\Sigma_\beta|^{-1/2} \exp((-1/2)\beta^\top \Sigma_\beta^{-1} \beta) (\sigma_p^2)^{-2-1} \exp(-\frac{2}{\sigma_p^2}). \end{aligned} \quad (3.2)$$

When formula (3.2) contains only one parameter to be estimated, the remaining parameters can be treated as constants, thereby eliminating them. Subsequently, a mixed sampling approach, comprising Gibbs and Metropolis-Hastings (MH) sampling, is employed for parameter estimation. The iterative procedure is outlined as follows:

Step 1: Initialize values $(\mathbf{W}_1^{*(0)}, \mathbf{W}_2^{*(0)}, \phi_1^{(0)}, \phi_0^{(0)}, \sigma_p^{2(0)})$ for the parameters \mathbf{W}_1^* , \mathbf{W}_2^* , ϕ_1 , ϕ_0 , σ_p^2 being evaluated.

Step 2: Set $l = 1$ and iterate through the parameters via the fully conditional posterior distribution:

- (1) Generate $\beta^{(l)}$ using $(\mathbf{W}_1^{*(l-1)}, \mathbf{W}_2^{*(l-1)}, \phi_1^{(l-1)}, \phi_0^{(l-1)}, \sigma_p^{2(l-1)})$ and the density

$$f(\beta|\cdot) \propto \exp(-1/2(\beta - V^{-1}U)^\top V(\beta - V^{-1}U)),$$

where $V = \sum_{t=1}^T X_t^\top \Sigma_P^{-1} X_t + \Sigma_\beta^{-1}$, $U = \sum_{t=1}^T X_t^\top \Sigma_P^{-1}(P_t - \mathbf{W}_1 - \mathbf{W}_2t)$.

- (2) Generate $\mathbf{W}_2^{*(l)}$ using $(\beta^{(l)}, \mathbf{W}_1^{*(l-1)}, \phi_1^{(l-1)}, \phi_0^{(l-1)}, \sigma_p^{2(l-1)})$ and the density

$$f(\mathbf{W}_2^*|\cdot) \propto \exp(-1/2(\mathbf{W}_2^* - V^{-1}U)^\top V(\mathbf{W}_2^* - V^{-1}U)),$$

where $V = (C_{\mathbf{W}_2^*})^{-1} + A_{\mathbf{W}_2^*}^\top \Sigma_P^{-1} A_{\mathbf{W}_2^*} \sum_{t=1}^T t^2$, $U = A_{\mathbf{W}_2^*}^\top \Sigma_P^{-1} \sum_{t=1}^T t(P_t - X_t\beta - \mathbf{W}_1)$.

- (3) Generate $\phi_0^{(l)}$ using $(\beta^{(l)}, \mathbf{W}_2^{*(l)}, \mathbf{W}_1^{*(l-1)}, \phi_1^{(l-1)}, \phi_0^{(l-1)}, \sigma_p^{2(l-1)})$ and the MH method, with the probability of acceptance ϕ_0^c defined as

$$h = \min\left(1, \frac{\prod_{t=1}^T \pi(P_t|\beta, \mathbf{W}_1, \mathbf{W}_2^*, \sigma_p^2, \phi_0^c) \pi(\mathbf{W}_2^*|\phi_0^c) \pi(\phi_0^c) g(\phi_0|\phi_0^c)}{\prod_{t=1}^T \pi(P_t|\beta, \mathbf{W}_1, \mathbf{W}_2^*, \sigma_p^2, \phi_0) \pi(\mathbf{W}_2^*|\phi_0) \pi(\phi_0) g(\phi_0^c|\phi_0)}\right),$$

where $g(\cdot|\cdot)$ is the proposal distribution.

- (4) Generate $\sigma_p^{2(l)}$ using $(\beta^{(l)}, \mathbf{W}_2^{*(l)}, \phi_0^{(l)}, \mathbf{W}_1^{*(l-1)}, \phi_1^{(l-1)})$ and the density

$$f(\sigma_p^2|\cdot) \propto (\sigma_p^2)^{2+nT/2} \exp\left(-\frac{2 + 1/2 \sum_{t=1}^T (P_t - X_t\beta - \mathbf{W}_1 - \mathbf{W}_2t)^\top (P_t - X_t\beta - \mathbf{W}_1 - \mathbf{W}_2t)}{\sigma_p^2}\right).$$

- (5) Generate $\mathbf{W}_1^{*(l)}$ using $(\beta^{(l)}, \mathbf{W}_2^{*(l)}, \phi_0^{(l)}, \sigma_p^{2(l)}, \phi_1^{(l-1)})$ and the density

$$f(\mathbf{W}_1^*|\cdot) \propto \exp(-1/2(\mathbf{W}_1^* - V^{-1}U)^\top V(\mathbf{W}_1^* - V^{-1}U)),$$

where $V = (C_{\mathbf{W}_1^*})^{-1} + T A_{\mathbf{W}_1^*}^\top \Sigma_P^{-1} A_{\mathbf{W}_1^*}$, $U = A_{\mathbf{W}_1^*}^\top \Sigma_P^{-1} \sum_{t=1}^T (P_t - X_t\beta - \mathbf{W}_2t)$.

- (6) Generate $\phi_1^{(l)}$ using $(\beta^{(l)}, \mathbf{W}_1^{*(l)}, \mathbf{W}_2^{*(l)}, \phi_0^{(l)}, \sigma_p^{2(l)}, \phi_1^{(l-1)})$ and the MH method, with the probability of acceptance ϕ_1^c defined as

$$r = \min\left(1, \frac{\prod_{t=1}^T \pi(P_t|\beta, \mathbf{W}_1^*, \mathbf{W}_2, \sigma_p^2, \phi_1^c) \pi(\mathbf{W}_1^*|\phi_1^c) \pi(\phi_1^c) g(\phi_1|\phi_1^c)}{\prod_{t=1}^T \pi(P_t|\beta, \mathbf{W}_1^*, \mathbf{W}_2, \sigma_p^2, \phi_1) \pi(\mathbf{W}_1^*|\phi_1) \pi(\phi_1) g(\phi_1^c|\phi_1)}\right),$$

where $g(\cdot|\cdot)$ is the proposal distribution.

Table 1. Parameter estimations of the simulation model.

Parameter	Preset	Estimation
β_0	1.01	1.02
β_1	-0.71	-0.71
β_2	0.72	0.72
β_3	-0.22	-0.21
ϕ_0	0.50	0.50
ϕ_1	2.00	2.00
σ_p^2	0.05	0.05

Step 3: Repeat Step 2 k times, with k being the total number of iterations.

Following the above procedure, we can obtain MCMC estimates for all model parameters.

4. Simulation

In this section, we perform simulations to evaluate the effectiveness of the proposed parameter estimation method for the RVF model. All the simulations are carried out using MATLAB. We configure the number of the annual precipitation monitoring stations and grid points of the predictive process as follows: $n = 1500$, $m = 16$, and $t = 60$. It's important to note that m is much smaller than n , maintaining a ratio of about 1:100. Striking this balance is essential since an excessively large value of m can hinder model performance, while an overly small m can lead to overfitting. Recognizing that the influence of altitude on annual precipitation is not apparent, we incorporate the altitude factor into the stochastic perturbation term within the RVF model. We set the maximum and minimum values of longitude and latitude in the low-dimensional space to be the same as those in the high-dimensional space and divide them equally into 16 grid points. Consequently, the simulation model is considered as

$$\begin{aligned} P(x, y, t) &= X\beta + \mathbf{W}_1(x, y) + \mathbf{W}_2(x, y)t + \eta(x, y, t) \\ &= \beta_0 + \beta_1x + \beta_2y + \beta_3t + \mathbf{W}_1(x, y) + \mathbf{W}_2(x, y)t + \eta(x, y, t), \end{aligned} \quad (4.1)$$

where $\beta = [\beta_0, \beta_1, \beta_2, \beta_3]'$ and $X = [L, x, y, t]$.

The model parameters are obtained by iterating 20,000 times, and the estimated values for the RVF model parameters are presented in Table 1. Based on the simulation results, it is evident that the estimated parameters closely approximate the preset parameter values. These results suggest that the parameter estimation method employed in this paper accurately fits the data and provides meaningful interpretations. Figure 1 displays the results from the final 19,000 iterations, encompassing seven parameters. Notably, it becomes apparent that all parameter iteration values stabilize around the 10,000th iteration, indicating convergence to a consistent state.

5. The data

We collect data from meteorological stations in six prominent countries across five continents to study global annual precipitation and its spatiotemporal dynamics. These datasets encompass critical information, including the number of monitoring stations, geographical coordinates, time, and precipitation to millimeter accuracy. The datasets vary in size from 114KB to 260MB. Specifically, we utilize data from 31 precipitation monitoring stations

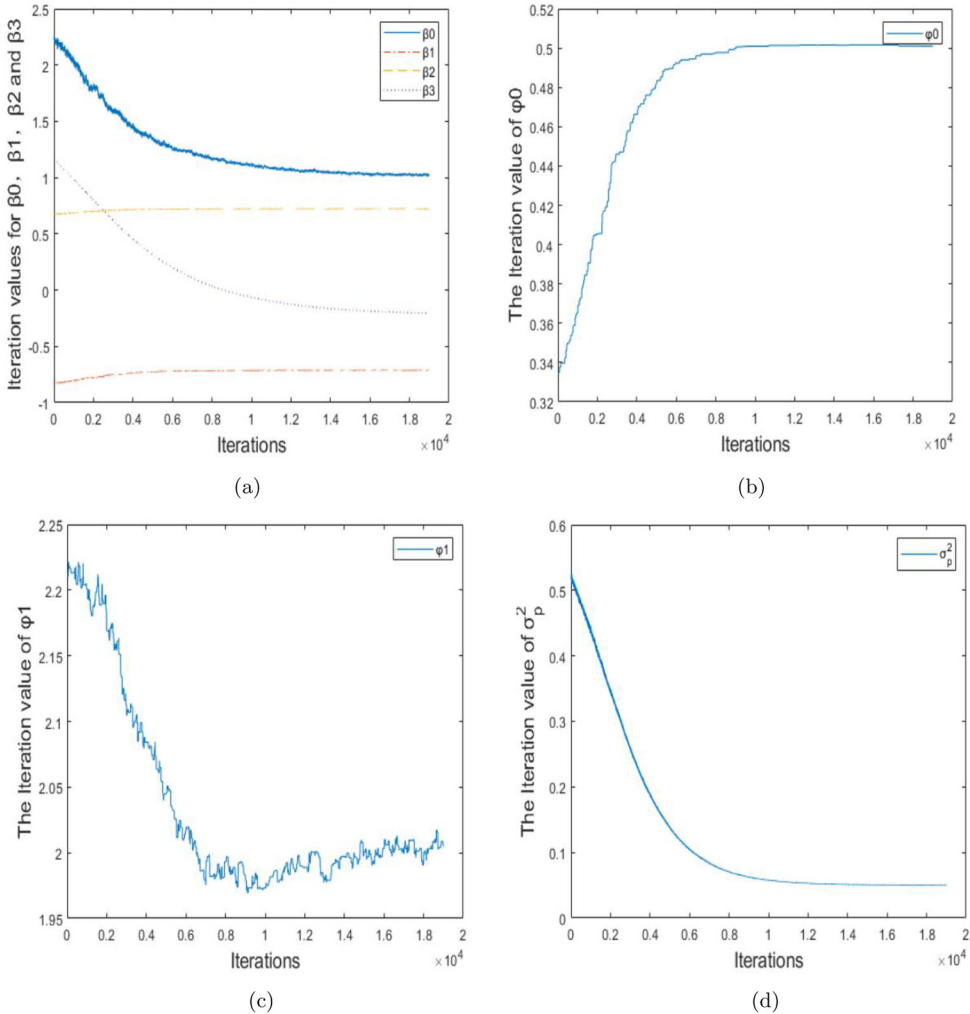


Figure 1. Results of 19,000 iterations on the parameters. (a) β , (b) ϕ_0 , (c) ϕ_1 , and (d) σ_p^2 .

covering 2004 to 2018 for China. For India, we analyze data from 35 precipitation monitoring stations covering 2000–2015. For the Netherlands, our dataset includes information from 32 monitoring stations from 2001 to 2016. For the United States, we focus on 98 precipitation monitoring stations in three states (Alabama, Mississippi, and Georgia) from 1999 to 2011. In addition, we examine data from 24 precipitation monitoring stations in Brazil, covering the years 1998 to 2017. Lastly, in the case of Australia, our dataset comprises 45 precipitation monitoring stations, covering the years 2009 to 2016. Table 2 provides a concise summary of the geographical distributions of these six countries, along with details regarding the number of monitoring locations, periods covered in the datasets, and the data sources. In practice, we use an equilateral conic projection to convert latitude and longitude into Cartesian coordinates. Figure 2 displays distribution maps of precipitation monitoring stations in these six countries, where the horizontal axis represents longitude, and the vertical axis corresponds to latitude.

Table 2. Basic information on the collected datasets.

Continent	Country	The number of sites	Selected period	Data sources
Asia	China	31	2004-2018	http://www.stats.gov.cn/tjsj/ndsj/
Asia	India	35	2000-2015	https://www.kaggle.com/rajanand/rainfall-in-india
Europe	Netherlands	32	2001-2016	https://www.kaggle.com/sinaasappel/historical-weather-in-the-netherlands-19012018
North America	the United States	98	1999-2011	https://www.kaggle.com/noaa/noaa-precipitation-15-minute
South America	Brazil	24	1998-2017	https://www.kaggle.com/fabiopotsch/precipitation-in-brazil
Oceania	Australia	45	2009-2016	https://www.kaggle.com/jsphyg/weather-dataset-rattle-package

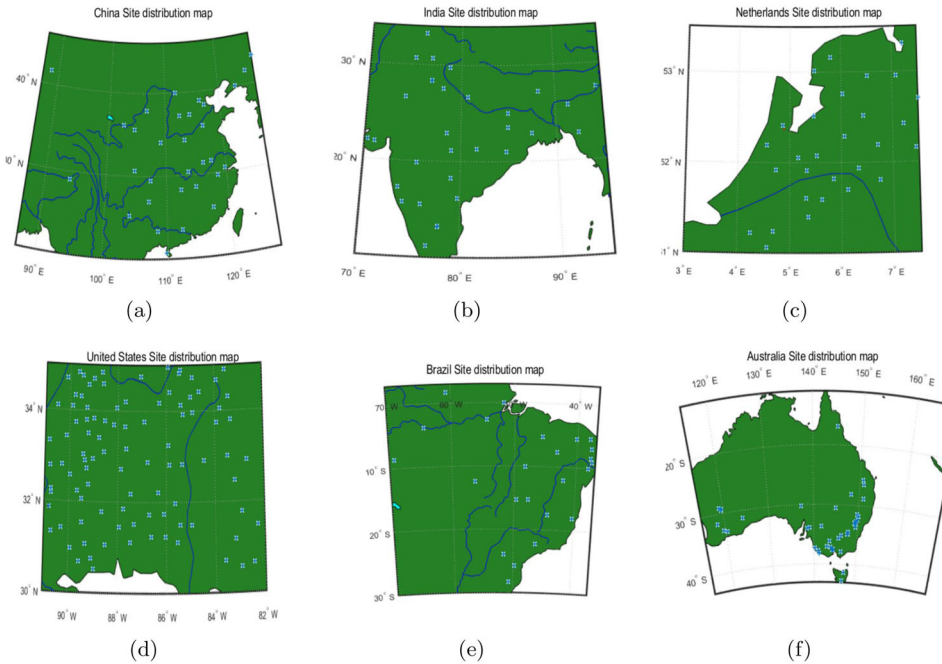
**Figure 2.** Geographical distributions of precipitation monitoring stations. (a) China, (b) India, (c) the Netherlands, (d) the United States, (e) Brazil, and (f) Australia.

Figure 3 shows the annual precipitation data from a single monitoring station in the six countries. The horizontal axis represents the year, while the vertical axis represents the precipitation depth. In this figure, the blue line represents each country's total annual mean precipitation intensity over the years, while the red line depicts the annual precipitation for each year. Examination of the datasets and Figure 3 reveals that the annual precipitation in each country has remained relatively stable in recent years. However, it is worth noting that there are significant variations in the total annual mean precipitation levels across different regions within each country.

6. Application

To assess the goodness of fit between models (2.8) and (2.9), we initially employ the AIC and BIC criteria. Specifically, we compare models' AIC and BIC values with different orders using

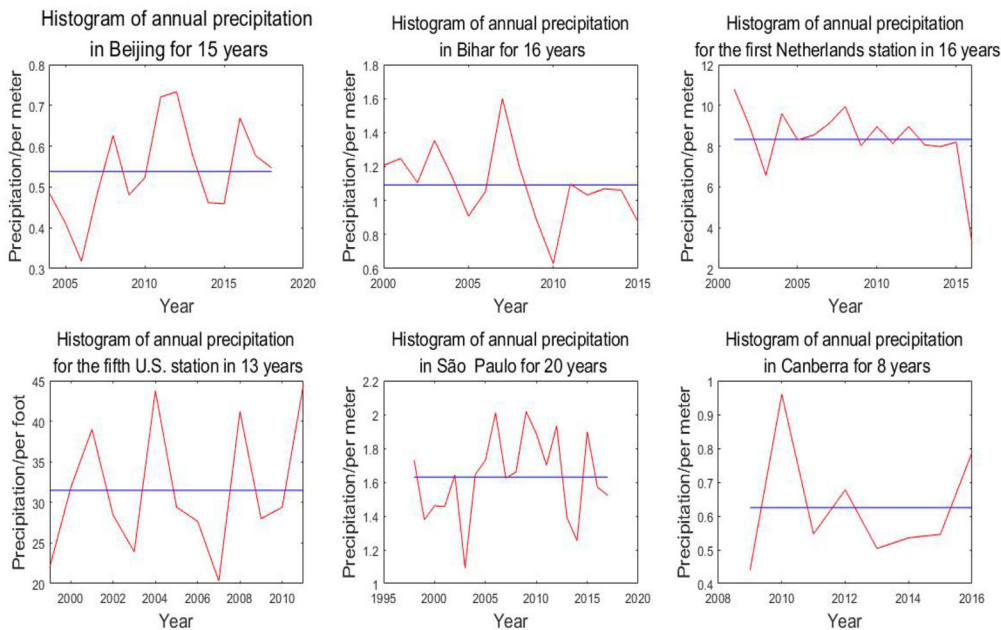


Figure 3. Line graphs of annual precipitation from selected precipitation monitoring stations in the six countries, arranged from left to right and top to bottom as China, India, the Netherlands, the United States, Brazil, and Australia.

Table 3. Comparison results of the models with different orders.

Model	AIC	BIC
$p = q = 0$	-830.50	-826.20
$p = q = 1$	-715.95	-705.91

the annual precipitation dataset from China, and the results are presented in Table 3. These criteria are denoted as

$$\text{AIC} = 2k - 2 \ln(L), \text{ and } \text{BIC} = k \ln(n) - 2 \ln(L),$$

where k represents the estimated number of parameters, L signifies the likelihood function, and n corresponds to the sample size. Upon examining the AIC and BIC values presented in Table 3, it is evident that the model with orders $p = q = 1$ exhibits smaller values. Consequently, we selected model (2.9) as the annual precipitation model for this study.

The datasets for the six countries are subjected to modeling and iteration using the provided estimation procedure for a total of 10,000 iterations, with the first half discarded. Subsequent posterior estimates of the model parameters are derived and presented in Table 4. Table 4 displays the format for the parameter β as (estimate, sd), where, for example, (-0.70, 0.13) indicates an estimate of -0.70 with a standard error of 0.13.

According to the obtained parameters, we have developed annual precipitation and RVF models for the six countries. Figure 4 depicts the maximum gradient direction of annual precipitation in some regions within these countries. The black point represents the starting point, while the red arrow indicates the direction of the maximum gradient. When an increasing trend in annual precipitation is observed, the direction of the arrow ensures a

Table 4. Estimated parameters for six countries.

Parameter	China	India	Netherlands	the United States	Brazil	Australia
β_0	(0.95,0.26)	(1.72,1.00)	(8.14,0.96)	(40.61,1.88)	(3.42,1.14)	(−0.14,0.28)
β_1	(−0.50,0.04)	(−0.47,0.16)	(0.06,0.17)	(−2.09,0.72)	(−0.31,0.22)	(0.43,0.08)
β_2	(0.02,0.16)	(0.68,0.23)	(0.13,0.18)	(−2.69,0.72)	(−0.11,0.18)	(0.13,0.23)
β_3	(0.02,0.10)	(−0.89,0.02)	(−0.05,0.01)	(0.42,0.61)	(5.37E-04,0.01)	(−0.01,0.04)
ϕ_0	6.76	2.13E-05	14.79	1.04	6.88	12.32
ϕ_1	1.25	0.87	21.95	10.08	0.53	6.61
σ_p^2	0.07	0.36	1.57	1.47E+02	0.28	0.10
W_1 range	(0.05,1.37)	(−2.57,0.94)	(−9.60E-06,0.10)	(−0.86,0.73)	(−1.73,0.04)	(−0.94,0.32)
W_2 range	(−0.02,0.01)	(0.89,0.89)	(−0.01,7.50E-09)	(−1.31,1.10)	(−0.10,0.03)	(−7.54E-10,0.08)

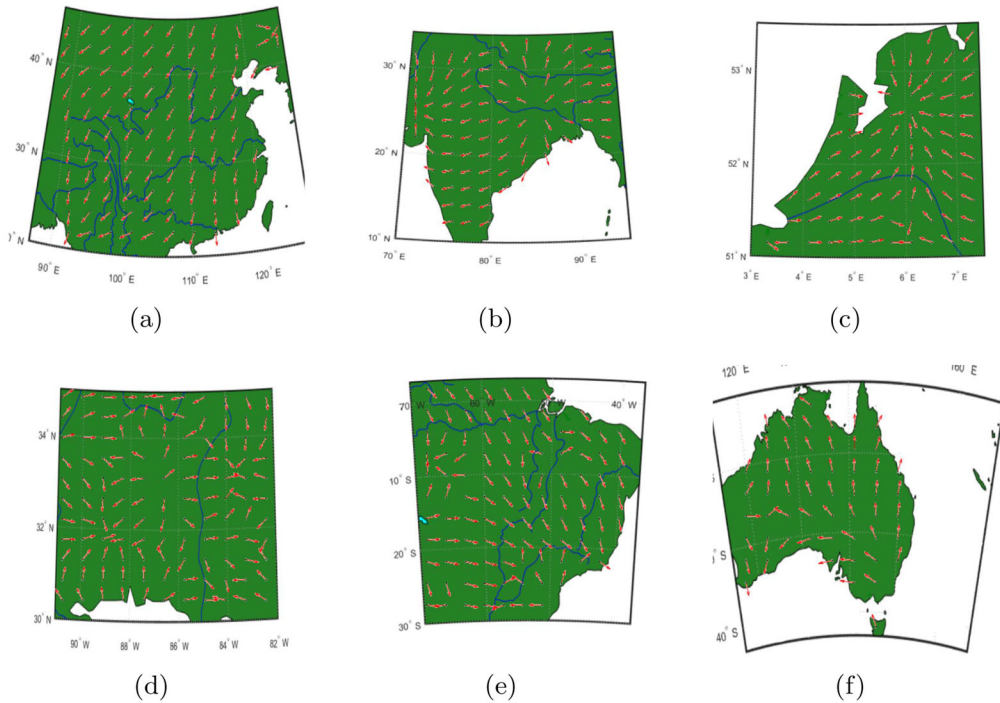


Figure 4. Maximum gradient direction of annual precipitation in parts of six countries. (a) China, (b) India, (c) the Netherlands, (d) the United States, (e) Brazil, and (f) Australia.

constant level of annual precipitation. Typically, this direction follows a trajectory from the coast to the interior.

The minimum velocity of any region can be calculated using Equation (2.4) after obtaining the direction of the maximum gradient. In the current maximum gradient direction, the annual precipitation velocity of this region will be the minimum in the future. If the minimum velocity is greater than 1, the future annual precipitation in this region will have a temporal velocity greater than its spatial velocity; conversely, if it is less than 1, the opposite is true.

Furthermore, six precipitation monitoring stations are used as examples to study and analyze the minimum velocity. Table 5 shows that the minimum velocities at the six selected monitoring stations are all less than 1, indicating that their temporal velocities are all less than their spatial velocities. The smallest temporal velocity is in Brazil, and the largest temporal and spatial velocities are both in the United States. The Netherlands has the largest minimum

Table 5. Minimum velocities for selected precipitation monitoring stations in six countries.

Parameter	China	India	Netherlands	the United States	Brazil	Australia
Temporal velocity	0.03	0.01	-0.04	0.64	-0.00	-0.02
Longitude velocity	-0.71	-1.07	0.24	3.33	-0.38	-0.04
Latitude velocity	-0.32	0.12	0.03	2.91	0.12	-0.29
Minimum velocity	0.04	0.01	-0.17	0.15	-0.01	-0.05

velocity. Interestingly, the temporal velocity is in the same direction as the minimum velocity, while the results are reversed for the United States and Australia. The temporal and spatial velocities of the United States are all positive, while those of Australia are all negative. In other words, in the current gradient direction, the annual precipitation of the United States is increasing, while that of Australia is decreasing. Regarding minimum velocity values, the Netherlands has the highest risk and the fastest change of the six regions. In addition, the annual precipitation is decreasing in the current gradient direction, suggesting that the region will likely face water scarcity in the future. Some preventive measures, such as improving water resource use efficiency and building reservoirs, can be taken in advance.

7. Conclusion

In this article, we develop an RVF model to predict the future annual precipitation velocity in different regions. The spatiotemporal gradient at any location can be calculated using the directional derivative, which allows us to obtain the annual precipitation velocity. We apply this RVF model to the annual precipitation data of six countries on five continents (China, India, the Netherlands, the United States, Brazil, and Australia) and obtain a good fitting effect, providing a satisfactory explanation for the dataset. When the intensity of precipitation in the current year increases, it indicates that the annual precipitation in the future will rise. If the increase is too large, one should expect floods and other disasters and take flood control and waterlogging prevention measures in advance. Conversely, water storage arrangements should be made. Additionally, we can analyze the maximum gradient direction of a certain location and obtain the minimum annual precipitation velocity. The minimum annual precipitation velocity indicates the rate of change of speed along the direction of the maximum annual precipitation gradient. If the minimum velocity is higher, it indicates that future annual precipitation will change rapidly, requiring the region to take measures for future industrial and agricultural production and to prepare for the possibility of natural disasters. This article has some limitations. To simplify the calculations, $f(t)$ is parameterized as a function of t . However, the model can be further extended to include additional terms, such as $f(t)$ being a function of t^2 , etc. The RVF model does not consider the relationship between temperature and precipitation or the influence of climate and mountains. Nevertheless, the model's overall performance is satisfactory, and it can be used in different regions of any country with relatively small spatial limitations.

Disclosure statement

No potential conflict of interest was reported by the author(s).

Funding

This document is the results of the research project funded by the Applied Basic Research Programs of Shanxi Province (Grant No. 201901D211105)

References

- Banerjee, S., A. E. Gelfand, A. O. Finley, and H. Sang. 2008. Gaussian predictive process models for large spatial data sets. *Journal of the Royal Statistical Society. Series B, Statistical Methodology* 70 (4):825–48. doi:10.1111/j.1467-9868.2008.00663.x. 19750209.
- Fischer, M., H. W. Rust, and U. Ulbrich. 2019. A spatial and seasonal climatology of extreme precipitation return-levels: A case study. *Spatial Statistics* 34:100275. doi:10.1016/j.spasta.2017.11.007.
- Furey, P. R., S. K. Kampf, J. S. Lanini, and A. Q. Dozier. 2012. A stochastic conceptual modeling approach for examining the effects of climate change on streamflows in mountain basins. *Journal of Hydrometeorology* 13 (3):837–55. doi:10.1175/JHM-D-11-037.1.
- Gu, M., J. Fei, and S. Sun. 2020. Online anomaly detection with sparse Gaussian processes. *Neurocomputing* 403:383–99. doi:10.1016/j.neucom.2020.04.077.
- Holsinger, L., R. E. Keane, D. J. Isaak, L. Eby, and M. K. Young. 2014. Relative effects of climate change and wildfires on stream temperatures: A simulation modeling approach in a Rocky Mountain watershed. *Climatic Change* 124 (1-2):191–206. doi:10.1007/s10584-014-1092-5.
- Liu, C., S. X. Yang, X. Li, L. Xu, and Lie. Deng. 2020. Noise level penalizing robust Gaussian process regression for NIR spectroscopy quantitative analysis. *Chemometrics and Intelligent Laboratory Systems* 201:104014. doi:10.1016/j.chemolab.2020.104014.
- Loarie, S. R., P. B. Duffy, H. Hamilton, G. P. Asner, C. B. Field, and D. D. Ackerly. 2009. The velocity of climate change. *Nature* 462 (7276):1052–5. doi:10.1038/nature08649. 20033047.
- Mahbod, M., and M. R. Rafiee. 2021. Trend analysis of extreme precipitation events across Iran using percentile indices. *International Journal of Climatology* 41 (2):952–69. doi:10.1002/joc.6708.
- Majumder, R., and B. J. Reich. 2023. A deep learning synthetic likelihood approximation of a non-stationary spatial model for extreme streamflow forecasting. *Spatial Statistics* 55:100755. doi:10.1016/j.spasta.2023.100755.
- Marques, I., N. Klein, and T. Kneib. 2020. Non-stationary spatial regression for modelling monthly precipitation in Germany. *Spatial Statistics* 40:100386. doi:10.1016/j.spasta.2019.100386.
- Mendes, J. M., K. F. Turkman, and J. Corte-Real. 2006. A Bayesian hierarchical model for local precipitation by downscaling large-scale atmospheric circulation patterns. *Environmetrics* 17 (7):721–38. doi:10.1002/env.790.
- Reis, D. S., and J. R. Stedinger. 2005. Bayesian MCMC flood frequency analysis with historical information. *Journal of Hydrology* 313 (1-2):97–116. doi:10.1016/j.jhydrol.2005.02.028.
- Rhode, S. 2020. Non-stationary Gaussian process regression applied in validation of vehicle dynamics models. *Engineering Applications of Artificial Intelligence* 93:103716. doi:10.1016/j.engappai.2020.103716.
- Ribas, A., J. Olcina, and D. Sauri. 2020. More exposed but also more vulnerable? Climate change, high intensity precipitation events and flooding in Mediterranean Spain. *Disaster Prevention and Management: An International Journal* 29 (3):229–48. doi:10.1108/DPM-05-2019-0149.
- Richards, J., J. A. Tawn, and S. Brown. 2023. Joint estimation of extreme spatially aggregated precipitation at different scales through mixture modelling. *Spatial Statistics* 53:100725. doi:10.1016/j.spasta.2022.100725.
- Rui, J., H. Zhang, Q. Ren, L. Yan, Q. Guo, and D. Zhang. 2020. TOC content prediction based on a combined Gaussian process regression model. *Marine and Petroleum Geology* 118:104429. doi:10.1016/j.marpetgeo.2020.104429.
- Rui, R., X. Li, L. Li, Q. Qin, and Y. Huang. 2020. Discrimination of driving factors of precipitation forms in Tianshan mountains area of China. *Journal of Arid Land Resources and Environment* 34:112–7. doi:10.13448/j.cnki.jalre.2020.73.

- Rusticucci, M., J. Marengo, O. Penalba, and M. Renom. 2010. An intercomparison of model-simulated in extreme rainfall and temperature events during the last half of the twentieth century. Part 1: mean values and variability. *Climatic Change* 98 (3-4):493–508. doi:10.1007/s10584-009-9742-8.
- Schliep, E. M., A. E. Gelfand, and J. S. Clark. 2015. Stochastic modeling for velocity of climate change. *Journal of Agricultural, Biological, and Environmental Statistics* 20 (3):323–42. doi:10.1007/s13253-015-0210-9.
- Sebille, Q., A.-L. Fougères, and C. Mercadier. 2017. Modeling extreme rainfall: A comparative study of spatial extreme value models. *Spatial Statistics* 21:187–208. doi:10.1016/j.spasta.2017.06.009.
- Sigrist, F., H. R. Künsch, and W. A. Stahel. 2011. An autoregressive spatio-temporal precipitation model. *Procedia Environmental Sciences* 3:2–7. doi:10.1016/j.proenv.2011.02.002.
- Sloat, M. R., B. B. Shepard, R. G. White, and S. Carson. 2005. Influence of stream temperature on the spatial distribution of westslope cutthroat trout growth potential within the Madison River Basin, Montana. *North American Journal of Fisheries Management* 25 (1):225–37. doi:10.1577/M03-165.1.
- Sørbye, S. H, and H. Rue. 2014. Scaling intrinsic Gaussian Markov random field priors in spatial modelling. *Spatial Statistics* 8:39–51. doi:10.1016/j.spasta.2013.06.004.
- Villarini, G., J. A. Smith, and F. Napolitano. 2010. Nonstationary modeling of a long record of rainfall and temperature over Rome. *Advances in Water Resources* 33 (10):1256–67. doi:10.1016/j.advwatres.2010.03.013.
- Zhang, X., W. D. Hogg, and Éva. Mekis. 2001. Spatial and temporal characteristics of heavy precipitation events over Canada. *Journal of Climate* 14 (9):1923–36. doi:10.1175/1520-0442(2001)014<1923:SATCOH>2.0.CO;2.